Available online at www.sciencedirect.com
SCIENCE DIRECT®
Journal of Computational Physics 190 (2003) 459–477
JOURNAL OF COMPUTATIONAL PHYSICS
www.elsevier.com/locate/jcp

Optimized prefactored compact schemes

Graham Ashcroft, Xin Zhang *

Department of Aeronautics and Astronautics, University of Southampton, Southampton, UK

Received 25 June 2002; received in revised form 15 May 2003; accepted 26 May 2003

Abstract

The numerical simulation of aeroacoustic phenomena requires high-order accurate numerical schemes with low dispersion and dissipation errors. In this paper we describe a strategy for developing high-order accurate prefactored compact schemes, requiring very small stencil support. These schemes require fewer boundary stencils and offer simpler boundary condition implementation than existing compact schemes. The prefactorization strategy splits the central implicit schemes into forward and backward biased operators. Using Fourier analysis, we show it is possible to select the coefficients of the biased operators such that their dispersion characteristics match those of the original central compact scheme and their numerical wavenumbers have equal and opposite imaginary components. This ensures that when the forward and backward stencils are added, the original central compact scheme is recovered. To extend the resolution characteristic of the schemes, an optimization strategy is employed in which formal order of accuracy is sacrificed in preference to enhanced resolution characteristics across the range of wavenumbers realizable on a given mesh. The resulting optimized schemes yield improved dispersion characteristics compared to the standard sixth- and eighth-order compact schemes making them more suitable for high-resolution numerical simulations in gas dynamics and computational aeroacoustics. The efficiency, accuracy and convergence characteristics of the new optimized prefactored compact schemes are demonstrated by their application to several test problems.

Keywords: Optimized compact differencing; High-order finite-difference; Computational aeroacoustics

1. Introduction

The field of computational aeroacoustics (CAA) has grown rapidly during the last decade due to a resurgence of interest in aeroacoustic phenomena driven by ever harsher legislation and increasing environmental awareness. CAA is concerned with the accurate numerical prediction of aerodynamically generated noise as well as its propagation and far-field characteristics. The inherently unsteady nature of aeroacoustic phenomena, the disparity in magnitude between mean and acoustic flow quantities, and the

* Corresponding author.
E-mail address: X.Zhang1@soton.ac.uk (X. Zhang).

0021-9991/$ - see front matter
doi:10.1016/S0021-9991(03)00293-6

high frequencies often encountered place stringent demands on the numerics [1]. The trend therefore within the field of CAA has been to employ higher-order accurate numerical schemes that have in some manner been optimized for wave propagation to reduce the required number of grid points per wavelength while still ensuring tolerable levels of numerical error.

Both the finite-volume and finite-difference methodologies have been adapted for this purpose [2–5]. However, as multidimensional finite-volume algorithms are generally more expensive in terms of numerical cost than finite-difference algorithms, the majority of CAA codes are based on the finite-difference methodology. Finite-difference schemes may be classified as either explicit or implicit. Explicit schemes employ large computational stencils for accuracy. By comparison, implicit (compact) schemes achieve high-order accuracy by solving for the spatial derivatives as independent variables at each grid point. For the same stencil width, compact schemes are known to exhibit significantly more resolution of the smaller scales than an equivalent explicit scheme. The drawback with these schemes is their implicit nature, which necessitates the solution of a linear system of equations to obtain the spatial derivative at any point. Generally, however, these systems are of a narrow-banded nature (usually tridiagonal) and may therefore be solved quite efficiently.

The focus of the present paper is a family of small-stencil compact schemes recently proposed by Hixon [6]. These schemes use a prefactorization method to reduce a non-dissipative central-difference stencil to two lower-order biased stencils which have easily solved reduced matrices. In [6] this approach was used to derive schemes of up to eighth-order accuracy requiring only three-point stencils. The advantages of these schemes over traditional compact schemes arise from their reduced stencil size and the independent nature of the resultant factored matrices. It is well known that a major difficulty in dealing with high-order finite-difference schemes is the formulation of stable stencils near boundaries. By reducing the stencil size of the compact schemes the prefactorization method reduces the required number of boundary stencils thereby simplifying boundary specification. As demonstrated in [6] the prefactorization also enhances robustness enabling the use of boundary stencils that would otherwise lead to unstable systems when used in conjunction with the unfactored scheme. The prefactored schemes also make boundary condition implementation much more straightforward than the standard schemes. As detailed in [6], this is a consequence of the $L+U$ factorization associated with the new schemes, which allows boundary corrections (e.g., to the normal derivative [7,8]) to be applied much more easily and efficiently than with an LU based scheme such as the Thomas algorithm.

In this work, we extend the factorization concept to a broader class of compact schemes using a more general derivation strategy. Rather than using the algebraic manipulations detailed in [6], we develop an approach that combines Fourier analysis with the notion of a numerical wavenumber. The advantage of this approach, alongside its more general nature, is that it ensures the application of an optimization strategy, designed to enhance the wave propagation characteristics of the schemes, is straightforward. Using this approach we derive two optimized fourth-order accurate prefactored compact schemes. The proposed schemes exhibit better wave propagation characteristics than the standard compact schemes, whilst retaining the advantages of the prefactored schemes.

The paper is organized as follows. In Section 2.1, a brief review of the compact differencing methodology is presented, along with a definition of the numerical wavenumber. In Section 2.2 the strategy for developing the prefactored schemes is described and a sample application is presented. The optimization of the prefactored schemes for wave propagation is presented in Section 2.3. Section 2.4 provides details of the boundary stencils for use with the interior schemes. The stability characteristics of the prefactored compact schemes in conjunction with the developed boundary closures are analysed in Section 3 through numerical applications and eigenvalue analysis. In Section 4 the favourable properties of the derived schemes are demonstrated through their application to several benchmark problems.

2. Scheme development

2.1. Compact discretization

Following Lele [9], a general compact approximation to the first spatial derivative $(\partial f/\partial x)$ may be written in the form:

$$\beta D_{i-2} + \alpha D_{i-1} + D_i + \alpha D_{i+1} + \beta D_{i+2} = c\frac{f_{i+3} - f_{i-3}}{6\Delta x} + b\frac{f_{i+2} - f_{i-2}}{4\Delta x} + a\frac{f_{i+1} - f_{i-1}}{2\Delta x}, \tag{1}$$

where D_i is the spatial derivative of the function f. The relations between the coefficients a, b, c, α and β are derived by matching the Taylor series coefficients of various orders. The first unmatched coefficient determines the formal truncation error of the approximation. These relations are:

$$a + b + c = 1 + 2\alpha + 2\beta \quad \text{(second order)}, \tag{2}$$

$$a + 2^2 b + 3^2 c = 2\frac{3!}{2!}(\alpha + 2^2\beta) \quad \text{(fourth order)}, \tag{3}$$

$$a + 2^4 b + 3^4 c = 2\frac{5!}{4!}(\alpha + 2^4\beta) \quad \text{(sixth order)}, \tag{4}$$

$$a + 2^6 b + 3^6 c = 2\frac{7!}{6!}(\alpha + 2^6\beta) \quad \text{(eighth order)}, \tag{5}$$

$$a + 2^8 b + 3^8 c = 2\frac{9!}{8!}(\alpha + 2^8\beta) \quad \text{(tenth order)}. \tag{6}$$

Only the eighth-order tridiagonal ($\beta = 0$) and the 10th-order pentadiagonal ($\beta \neq 0$) schemes have unique coefficients. The other lower-order schemes have free coefficients that are not determined until more constraints are imposed or the stencil size is reduced. In the following work we consider only tridiagonal systems ($\beta = 0$), however the application of the analysis to pentadiagonal schemes is straightforward.

The numerical wavenumber of the generic compact derivative defined in Eq. (1) is determined using Fourier analysis. The Fourier transform and its inverse are related by

$$\tilde{f}(\kappa) = \frac{1}{2\pi}\int_{-\infty}^{\infty} f(x)\mathrm{e}^{-\mathrm{i}\kappa x}\,\mathrm{d}\kappa, \tag{7}$$

$$f(x) = \int_{-\infty}^{\infty} \tilde{f}(\kappa)\mathrm{e}^{\mathrm{i}\kappa x}\,\mathrm{d}x. \tag{8}$$

Taking the Fourier transform of both sides of Eq. (1) and through the use of Euler's formula we find

$$\mathrm{i}\kappa\tilde{f} = \frac{\mathrm{i}}{\Delta x}\left(\frac{a\sin(\kappa\Delta x) + (b/2)\sin(2\kappa\Delta x) + (c/3)\sin(3\kappa\Delta x)}{1 + 2\alpha\cos(\kappa\Delta x) + 2\beta\cos(2\kappa\Delta x)}\right)\tilde{f}. \tag{9}$$

Comparing the two sides of the above equation it is clear that the quantity

$$\tilde{\kappa} = \frac{1}{\Delta x}\left(\frac{a\sin(\kappa\Delta x) + (b/2)\sin(2\kappa\Delta x) + (c/3)\sin(3\kappa\Delta x)}{1 + 2\alpha\cos(\kappa\Delta x) + 2\beta\cos(2\kappa\Delta x)}\right) \tag{10}$$

is the effective (or numerical) wavenumber of the Fourier transformation of the compact finite difference scheme. We may observe immediately that the numerical wave number is purely real. This is a property of symmetric operators and indicates the scheme is non-dissipative. It may also be observed that the numerical wave number provides a good approximation of the actual wavenumber only over a limited portion of the wavenumber spectrum [9, Fig. 1].

2.2. Prefactored compact schemes

To derive the factorized compact schemes we begin in the same manner as Hixon [10] and define forward and backward operators D_i^{F} and D_i^{B}, such that

$$D_i = \frac{1}{2}(D_i^{\mathrm{F}} + D_i^{\mathrm{B}}). \tag{11}$$

The generic stencils for the forward and backward derivative operators are then defined as:

$$\alpha_{\mathrm{F}} D_{i+1}^{\mathrm{F}} + \beta_{\mathrm{F}} D_i^{\mathrm{F}} = \frac{1}{\Delta x}[a_{\mathrm{F}} f_{i+2} + b_{\mathrm{F}} f_{i+1} + c_{\mathrm{F}} f_i + d_{\mathrm{F}} f_{i-1} + e_{\mathrm{F}} f_{i-2}], \tag{12}$$

$$\beta_{\mathrm{B}} D_i^{\mathrm{B}} + \gamma_{\mathrm{B}} D_{i-1}^{\mathrm{B}} = \frac{1}{\Delta x}[a_{\mathrm{B}} f_{i+2} + b_{\mathrm{B}} f_{i+1} + c_{\mathrm{B}} f_i + d_{\mathrm{B}} f_{i-1} + e_{\mathrm{B}} f_{i-2}], \tag{13}$$

where the coefficients must be chosen such that when the two biased stencils are added, the original central compact scheme is recovered. To achieve this we refer to the analysis presented by Hixon and Turkel [11], which revealed a property of their compact MacCormack schemes to be that the real (dispersive) components of the numerical wavenumbers of the forward and backward stencils are equal and identical to the numerical wavenumber of the original central compact scheme, whilst the imaginary (dissipative) components of the numerical wavenumbers are equal and opposite. It is this property that we exploit to develop the schemes presented in this paper. That is, to ensure we recover the original (non-dissipative) compact scheme when the biased operators are added, the coefficients of the forward and backward stencils are chosen such that the imaginary components of the numerical wavenumbers of the forward and backward stencils are equal and opposite, and the real components are equal and identical to the numerical wavenumber of the original scheme.

The numerical wavenumber of the generic compact stencil (1) has already been presented in Eq. (10). The numerical wavenumbers of the generic forward and backward operators may be determined in a similar manner. The real and imaginary components of the numerical wavenumber, of the generic forward stencil defined by Eq. (12), are given by:

$$\begin{aligned}\mathrm{Re}(\tilde{\kappa}_{\mathrm{F}}\Delta x) = {} & \frac{(a_{\mathrm{F}}\alpha_{\mathrm{F}} + b_{\mathrm{F}}\beta_{\mathrm{F}} - c_{\mathrm{F}}\alpha_{\mathrm{F}} - d_{\mathrm{F}}\beta_{\mathrm{F}})\sin(\kappa\Delta x)}{\alpha_{\mathrm{F}}^2 + \beta_{\mathrm{F}}^2 + 2\alpha_{\mathrm{F}}\beta_{\mathrm{F}}\cos(\kappa\Delta x)} \\ & + \frac{(a_{\mathrm{F}}\beta_{\mathrm{F}} - d_{\mathrm{F}}\alpha_{\mathrm{F}} - e_{\mathrm{F}}\beta_{\mathrm{F}})\sin(2\kappa\Delta x) - e_{\mathrm{F}}\alpha_{\mathrm{F}}\sin(3\kappa\Delta x)}{\alpha_{\mathrm{F}}^2 + \beta_{\mathrm{F}}^2 + 2\alpha_{\mathrm{F}}\beta_{\mathrm{F}}\cos(\kappa\Delta x)},\end{aligned} \tag{14}$$

$$\begin{aligned}\mathrm{Im}(\tilde{\kappa}_{\mathrm{F}}\Delta x) = {} & \frac{-(b_{\mathrm{F}}\alpha_{\mathrm{F}} + c_{\mathrm{F}}\beta_{\mathrm{F}}) - (a_{\mathrm{F}}\alpha_{\mathrm{F}} + b_{\mathrm{F}}\beta_{\mathrm{F}} + c_{\mathrm{F}}\alpha_{\mathrm{F}} + d_{\mathrm{F}}\beta_{\mathrm{F}})\cos(\kappa\Delta x)}{\alpha_{\mathrm{F}}^2 + \beta_{\mathrm{F}}^2 + 2\alpha_{\mathrm{F}}\beta_{\mathrm{F}}\cos(\kappa\Delta x)} \\ & - \frac{(a_{\mathrm{F}}\beta_{\mathrm{F}} + d_{\mathrm{F}}\alpha_{\mathrm{F}} + e_{\mathrm{F}}\beta_{\mathrm{F}})\cos(2\kappa\Delta x) + e_{\mathrm{F}}\alpha_{\mathrm{F}}\cos(3\kappa\Delta x)}{\alpha_{\mathrm{F}}^2 + \beta_{\mathrm{F}}^2 + 2\alpha_{\mathrm{F}}\beta_{\mathrm{F}}\cos(\kappa\Delta x)}\end{aligned} \tag{15}$$

and those for the backward stencil defined by Eq. (13), by:

$$\mathrm{Re}(\tilde{\kappa}_{\mathrm{B}}\Delta x) = \frac{(b_{\mathrm{B}}\beta_{\mathrm{B}} + c_{\mathrm{B}}\gamma_{\mathrm{B}} - d_{\mathrm{B}}\beta_{\mathrm{B}} - e_{\mathrm{B}}\gamma_{\mathrm{B}})\sin(\kappa\Delta x)}{\beta_{\mathrm{B}}^2 + \gamma_{\mathrm{B}}^2 + 2\gamma_{\mathrm{B}}\beta_{\mathrm{B}}\cos(\kappa\Delta x)} + \frac{(a_{\mathrm{B}}\beta_{\mathrm{B}} + b_{\mathrm{B}}\gamma_{\mathrm{B}} - e_{\mathrm{B}}\beta_{\mathrm{B}})\sin(2\kappa\Delta x) + a_{\mathrm{B}}\gamma_{\mathrm{B}}\sin(3\kappa\Delta x)}{\beta_{\mathrm{B}}^2 + \gamma_{\mathrm{B}}^2 + 2\gamma_{\mathrm{B}}\beta_{\mathrm{B}}\cos(\kappa\Delta x)}, \tag{16}$$

$$\mathrm{Im}(\tilde{\kappa}_{\mathrm{B}}\Delta x) = \frac{-(c_{\mathrm{B}}\beta_{\mathrm{B}} + d_{\mathrm{B}}\gamma_{\mathrm{B}}) - (b_{\mathrm{B}}\beta_{\mathrm{B}} + c_{\mathrm{B}}\gamma_{\mathrm{B}} + d_{\mathrm{B}}\beta_{\mathrm{B}} + e_{\mathrm{B}}\gamma_{\mathrm{B}})\cos(\kappa\Delta x)}{\beta_{\mathrm{B}}^2 + \gamma_{\mathrm{B}}^2 + 2\gamma_{\mathrm{B}}\beta_{\mathrm{B}}\cos(\kappa\Delta x)} - \frac{(a_{\mathrm{B}}\beta_{\mathrm{B}} + b_{\mathrm{B}}\gamma_{\mathrm{B}} + e_{\mathrm{B}}\beta_{\mathrm{B}})\cos(2\kappa\Delta x) + a_{\mathrm{B}}\gamma_{\mathrm{B}}\cos(3\kappa\Delta x)}{\beta_{\mathrm{B}}^2 + \gamma_{\mathrm{B}}^2 + 2\gamma_{\mathrm{B}}\beta_{\mathrm{B}}\cos(\kappa\Delta x)}. \tag{17}$$

From these relationships we observe it is sufficient to impose the following restrictions on the coefficients of the backward stencil to ensure the imaginary components of the forward and backward operators are equal and opposite

$$\begin{aligned} &\beta_{\mathrm{B}} = \beta_{\mathrm{F}}, \quad \gamma_{\mathrm{B}} = \alpha_{\mathrm{F}}, \quad a_{\mathrm{B}} = -e_{\mathrm{F}}, \\ &b_{\mathrm{B}} = -d_{\mathrm{F}}, \quad c_{\mathrm{B}} = -c_{\mathrm{F}}, \quad d_{\mathrm{B}} = -b_{\mathrm{F}}, \quad e_{\mathrm{B}} = -a_{\mathrm{F}}. \end{aligned} \tag{18}$$

The coefficients of the forward stencil may now be determined by matching the various terms in Eq. (14) with those in Eq. (10), and by introducing the relation $a_{\mathrm{F}} + b_{\mathrm{F}} + c_{\mathrm{F}} + d_{\mathrm{F}} + e_{\mathrm{F}} = 0$ to ensure that in regions of zero gradient the computed derivatives vanish.

To demonstrate the procedure we consider the following sixth-order compact scheme

$$\frac{1}{5}(D_{i+1} + D_{i-1}) + \frac{3}{5}D_i = \frac{1}{\Delta x}\left[\frac{1}{60}(f_{i+2} - f_{i-2}) + \frac{14}{30}(f_{i+1} - f_{i-1})\right]. \tag{19}$$

With reference to Eq. (10) we see that the numerical wavenumber is given by:

$$\tilde{\kappa}\Delta x = \frac{\frac{14}{15}\sin(\kappa\Delta x) + \frac{1}{30}\sin(2\kappa\Delta x)}{\frac{3}{5} + \frac{2}{5}\cos(\kappa\Delta x)}. \tag{20}$$

A comparison of this equation with Eq. (14) indicates it is sufficient to consider a simplified form of the generic forward biased stencil (with $a_{\mathrm{F}} = e_{\mathrm{F}} = 0$) to replicate this scheme's characteristics. The coefficients are then obtained by solving the following system of equations:

$$\begin{aligned} &\alpha_{\mathrm{F}}^2 + \beta_{\mathrm{F}}^2 = 0.6, \quad 2\alpha_{\mathrm{F}}\beta_{\mathrm{F}} = 0.4, \\ &b_{\mathrm{F}}\beta_{\mathrm{F}} - d_{\mathrm{F}}\beta_{\mathrm{F}} - c_{\mathrm{F}}\alpha_{\mathrm{F}} = 0.9333\dot{3}, \quad -d_{\mathrm{F}}\alpha_{\mathrm{F}} = 0.0333\dot{3}, \\ &b_{\mathrm{F}} + c_{\mathrm{F}} + d_{\mathrm{F}} = 0.0. \end{aligned} \tag{21}$$

Due to the quadratic terms in the first of these relations, the coefficients are not uniquely determined by the above system alone. To choose from the range of possible coefficients, we note from [10] that any error ϵ_0 in the boundary derivative propagates into the domain as

$$\varepsilon_i = \left(\frac{\alpha_{\mathrm{F}}}{\beta_{\mathrm{F}}}\right)^i \varepsilon_0, \tag{22}$$

where ε_i denotes the error at the ith point from the boundary. From the range of possible values we therefore select those for which the ratio $\alpha_{\mathrm{F}}/\beta_{\mathrm{F}}$ is a minimum in order to minimize the influence of errors at

Table 1
Prefactored scheme coefficients

	6/6 Scheme	6/4 Scheme	8/4 Scheme
α_F	0.27639320225002103	0.29749586350149729	0.36469246438579827
β_F	0.72360679761913232	0.71518963303413346	0.68337354822981936
a_F	0.0	0.0	0.0
b_F	0.87939886714173305	0.87203153537225117	0.80189188343264239
c_F	−0.75879773418340322	−0.73137757420887159	−0.53899133241291931
d_F	−0.12060113295832982	−0.14065396116337958	−0.27962697285647092
e_F	0.0	0.0	0.01672642183674783

the boundaries on the interior scheme. The final coefficients are given in Table 1. Here 6/6, 6/4 and 8/4 denote the various schemes developed in this work. The first digit refers to the maximum order of accuracy of the scheme, while the second refers to the actual order of accuracy following optimization (to be defined in the following section). The un-optimized sixth-order scheme is therefore denoted 6/6. It may be observed that in relation to the original centered scheme the stencil has been reduced from five points to three points, and the original tridiagonal matrix has been replaced by two independent bidiagonal matrices. This scheme is identical to the sixth-order scheme presented in [10].

2.3. Optimized prefactored compact schemes

Discretization schemes that sacrifice formal order of accuracy in favour of wide-band performance can provide significantly better wave propagation characteristics in the high wavenumber range. It is this strategy we now develop for the prefactored compact schemes. Following Kim and Lee [12] we define the integrated error (weighted deviation) as

$$\mathrm{Err} \equiv \int_0^{r\pi} (\kappa\Delta x - \tilde{\kappa}\Delta x)^2 W(\kappa\Delta x)\,\mathrm{d}(\kappa\Delta x), \tag{23}$$

where $W(\kappa\Delta x)$ is a weighting function, and r is a factor to determine the optimization range $(0 < r < 1)$ under consideration. The integrated error defined in Eq. (23) is different from that of Tam and Webb [4] in that it contains the weighting function and range factor r. The weight function in Eq. (23) makes the equation analytically integrable and also allows the integrand to be weighted to the high wavenumber range. The weighting function employed in this paper, follows that proposed Kim and Lee, which has the form

$$W(\kappa\Delta x) = [1 + 2\alpha\cos(\kappa\Delta x) + 2\beta\cos(2\kappa\Delta x)]^2, \tag{24}$$

where the parameters α and β correspond to those defined in Eq. (1). The conditions for Err to be a minimum are

$$\frac{\partial \mathrm{Err}}{\partial \eta_i} = 0 \quad \text{for } i = 1, 2, \ldots, 5, \tag{25}$$

where $\eta_1 = a$, $\eta_2 = b$, $\eta_3 = c$, $\eta_4 = \alpha$ and $\eta_5 = \beta$, again correspond to the coefficients of the basic stencil as defined by Eq. (1). When combined with Eqs. (2) and (3) (to maintain at least fourth-order accuracy) we obtain a system of linear algebraic equations by which the optimal coefficients may be obtained.

We consider the application of this optimization strategy to the sixth-order scheme described previously and the following formally eighth-order accurate scheme:

$$\alpha(D_{i+1}+D_{i-1})+D_i=\frac{1}{2\Delta x}\left[\frac{c}{3}(f_{i+3}-f_{i-3})+\frac{b}{2}(f_{i+2}-f_{i-2})+a(f_{i+1}-f_{i-1})\right], \tag{26}$$

where $a=\frac{1}{6}(\alpha+9)$, $b=\frac{1}{13}(32\alpha-9)$, $c=\frac{1}{10}(-3\alpha+1)$ and $\alpha=\frac{3}{8}$ for eighth-order accuracy. When, however, we require only fourth-order accuracy we have a two parameter family defined by $a=\frac{1}{3}(2\alpha+5c+4)$ and $b=\frac{1}{3}(4\alpha-8c-1)$. In this case two of the relations from Eq. (25) are employed to close the system of equations and determine the coefficients. A similar strategy is employed for the formally sixth-order scheme. However, in this case we only have a single free parameter for optimization when we stipulate fourth-order accuracy, and therefore utilize only one of the relations from Eq. (25) to perform the optimization.

The application of this procedure to the formally sixth-order scheme defined by Eq. (19), and the formally eighth-order scheme defined by Eq. (26) leads to the two optimized prefactored schemes defined by the coefficients given in Table 1. The first of these scheme requires a three-point stencil, whereas the latter requires a five-point stencil. The fourth-order three-point stencil retains the same stencil size as the un-optimized sixth-order prefactored compact scheme, and therefore requires the same computational effort, however it has improved resolution characteristics. The second scheme also retains the desirable bi-diagonal nature and requires only one additional point to compute the forward and backward stencils. In relation to the original eighth-order scheme the stencil size has been reduced by two points. The relationships between $\tilde{\kappa}\Delta x$ and $\kappa\Delta x$ over the interval 0 to π for these schemes are shown in Fig. 1 alongside those for the un-optimized sixth-order prefactored compact scheme, and the well known fourth-order DRP scheme of Tam and Webb [4]. The dispersive characteristics of these schemes may be more clearly seen in Fig. 2, which shows phase speed error ($|(\mathrm{d}(\tilde{\kappa}\Delta x)/\mathrm{d}(\kappa\Delta x))-1.0|$) as a function of wave number on a logarithmic scale. The optimized schemes maintain a low dispersive error over a larger range of wavenumbers. For $\kappa\Delta x$ up to almost 1.4 the fourth-order, three-point stencil maintains the error below the 10^{-3} level. The fourth-order, five-point stencil performs even better, maintaining this low level of error up to $\kappa\Delta x \simeq 1.9$. The optimized schemes all exhibit greater dispersion errors for long waves, however the magnitude of these

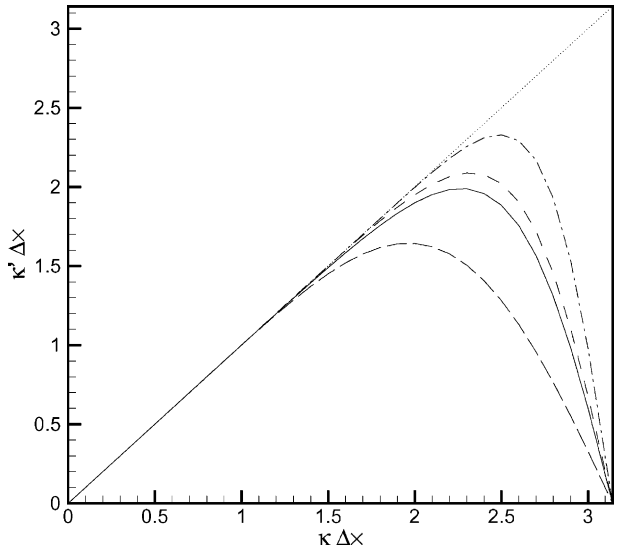

Fig. 1. Dispersive characteristics of schemes. (···) Ideal relationship, (– – –) fourth-order DRP scheme (seven-point stencil), (—) sixth-order compact scheme (three-point stencil), (- - -) fourth-order compact scheme (three-point stencil), (– · – · –) fourth-order compact scheme (five-point stencil).

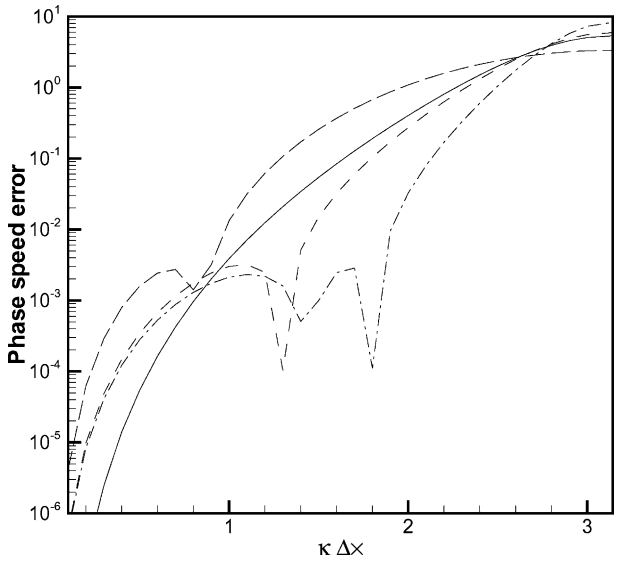

Fig. 2. Phase speed error on a logarithmic scale. (– – –) Fourth-order DRP scheme (seven-point stencil), (—) sixth-order compact scheme (three-point stencil), (- - -) fourth-order compact scheme (three-point stencil), (– · – · –) fourth-order compact scheme (five-point stencil).

errors remains very small. Further characteristics of these schemes are summarized in Table 2. Here, $\tilde{\kappa}_c \Delta x$ denotes the maximum resolvable wavenumber using the criterion $(|(\mathrm{d}(\tilde{\kappa}\Delta x)/\mathrm{d}(\kappa\Delta x) - 1.0)|) < 0.005$. The resolution of the spatial discretization schemes is also represented by the minimum points-per-wavelength needed to resolve a wave. Here the points-per-wavelength value has been computed as $2\pi/\tilde{\kappa}_c \Delta x$. The maximum effective wavenumber is indicated by $\tilde{\kappa}_{\max} \Delta x$.

2.4. Boundary formulations

For a domain consisting of N points, the three-point, fourth-order scheme can be applied from $j = 2$ to $N - 1$, while the five-point, fourth-order scheme can be applied from $j = 3$ to $N - 2$. At and near the domain boundaries it is therefore necessary to employ additional expressions. Furthermore, in realistic computations similar boundary stencils are also needed along inter-block boundaries in multi-block calculations. In contrast to the situation along external domain boundaries, however, the flow data are known on both sides of the boundary in such situations. Two forms of explicit boundary stencils have therefore been developed. Along internal boundaries a central explicit stencil is employed, whereas along external boundaries a biased explicit stencil is used.

Table 2
Points-per-wavelength required to satisfy $((|\mathrm{d}(\tilde{\kappa}\Delta x)/\mathrm{d}(\kappa\Delta x)) - 1.0|) < 0.005$

Spatial discretization	Stencil size	$\tilde{\kappa}_c \Delta x$	Resolution	$\tilde{\kappa}_{\max} \Delta x$
Explicit (Δx^2)	3	0.10	62.83	1.00
Explicit DRP (Δx^4)	7	0.92	6.83	1.64
PF compact (Δx^6)	3	1.03	6.10	1.98
PF compact (Δx^4)	3	1.40	4.49	2.09
PF compact (Δx^4)	5	1.85	3.40	2.48

The biased derivative operators for use with the three-point, fourth-order scheme are:

$$D_1^{\mathrm{B}} = \frac{1}{\Delta x}\sum_{j=1}^{4} s_j f_j, \quad D_N^{\mathrm{B}} = \frac{1}{\Delta x}\sum_{j=N-3}^{N} e_j f_j, \tag{27}$$

and

$$D_1^{\mathrm{F}} = \frac{1}{\Delta x}\sum_{j=1}^{4} -e_{N+1-j} f_j, \quad D_N^{\mathrm{F}} = \frac{1}{\Delta x}\sum_{j=N-3}^{N} -s_{N+1-j} f_j, \tag{28}$$

where the coefficients s_j and e_j have been determined by matching the Taylor series of the forward and backward compact interior stencils to third-order accuracy. The numerical values of the coefficients are listed in Tables 3 and 4. Along internal boundaries the following skewed 11 point central schemes are employed:

$$D_i^{\mathrm{F}} = \frac{1}{\Delta x}\sum_{j=-5}^{5} b_j f_{i+j}, \quad D_i^{\mathrm{B}} = \frac{1}{\Delta x}\sum_{j=-5}^{5} -b_{-j} f_{i+j}, \tag{29}$$

where the coefficients b_j are as listed in Table 5. These coefficients have been determined by matching the Taylor series expansions of the forward and backward interior stencils to fourth-order and using the remaining free coefficients to more closely match the dispersion characteristics of these stencils with those of the interior scheme.

For the optimized five-point fourth-order scheme, boundary stencils are required at nodes $j = 1,\ j = 2,\ j = N-1$ and $j = N$. At points $j = 2$ and $j = N-1$ the biased explicit stencils must provide approximations of D^{F} and D^{B}. The coefficients of the biased explicit stencils use at these points have been obtained by matching the Taylor series expansions of the explicit stencils to those of the forward and backward derivative operators to third-order. The resulting boundary stencils are:

$$D_2^{\mathrm{B}} = \frac{1}{\Delta x}\sum_{j=1}^{4} s_j f_j, \quad D_{N-1}^{\mathrm{B}} = \frac{1}{\Delta x}\sum_{j=N-3}^{N} e_j f_j, \tag{30}$$

Table 3
Boundary stencil coefficients

	8/4 Scheme	6/4 Scheme
s_1	−0.266441396584756	−1.968010730879214299
s_2	−0.633783873497153	3.336693493864702415
s_3	1.066891936748576	−1.769354795091761932
s_4	−0.16666666666666	0.400672032106273816

Table 4
Boundary stencil coefficients

	8/4 Scheme	6/4 Scheme
e_N	0.400225270081910	1.69865593578745236
e_{N-1}	0.366216126502846	−2.66330650613529758
e_{N-2}	−0.933108063251423	1.23064520490823806
e_{N-3}	0.1666666666666666	−0.26599463456039285

Table 5
Boundary stencil coefficients

	6/4 Scheme	8/4 Scheme
b_{-5}	−0.00083442741566041	−0.00390419271986273
b_{-4}	0.01022630353651893	0.02780538036220911
b_{-3}	−0.05956199104811759	−0.10589163462457388
b_{-2}	0.22724621139300842	0.29755042262117544
b_{-1}	−0.72224477117316119	−0.91725943599549454
b_0	−0.21013712054967647	0.07750687358345097
b_1	0.96979343766394390	0.85851156238327769
b_2	−0.27390976718640895	−0.31630942259240957
b_3	0.07031776392683924	0.10589163462457388
b_4	−0.01184575620106222	−0.02780538036220911
b_5	0.00095011705377633	0.00390419271986273

and

$$D_2^{\mathrm{F}} = \frac{1}{\Delta x}\sum_{j=1}^{4} -e_{N+1-j} f_j, \quad D_{N-1}^{\mathrm{F}} = \frac{1}{\Delta x}\sum_{j=N-3}^{N} -s_{N+1-j} f_j, \tag{31}$$

where coefficients s_j and e_j are as listed in Tables 3 and 4. At the actual boundary points $j = 1$ and $j = N$, additional relations are required. At these points the following third-order explicit stencil is used:

$$D_1 = \frac{1}{\Delta x}\sum_{j=1}^{4} c_j f_j, \quad D_N = \frac{1}{\Delta x}\sum_{j=N-3}^{N} -c_{N+1-j} f_j, \tag{32}$$

where $c_1 = -33/18, c_2 = 3, c_3 = -3/2$ and $c_4 = 1/3$. Along internal boundaries, the same 11-point stencil (29) as used with the fourth-order three-point interior scheme is used, but with the coefficients as defined in Table 5.

3. Scheme analysis

The computational cost of the optimized prefactored compact schemes is an important consideration. The optimization procedure itself does not incur any additional computational costs. The optimized schemes therefore require the same computational effort as the un-optimized schemes. The prefactorization does, however, incur a small computational penalty. To see this we first note that either of the optimized prefactored fourth-order schemes may be written in the form:

$$\frac{1}{2}D_j^{\mathrm{F}} = \frac{1}{2\beta_{\mathrm{F}}\Delta x}\left[b_{\mathrm{F}}(f_{j+1} - f_j) + d_{\mathrm{F}}(f_{j-1} - f_j) + e_{\mathrm{F}}(f_{j-2} - f_j)\right] - \frac{\alpha_{\mathrm{F}}}{2\beta_{\mathrm{F}}} D_{j+1}^{\mathrm{F}}, \tag{33}$$

$$\frac{1}{2}D_j^{\mathrm{B}} = \frac{1}{2\beta_{\mathrm{F}}\Delta x}\left[b_{\mathrm{F}}(f_j - f_{j-1}) + d_{\mathrm{F}}(f_j - f_{j+1}) + e_{\mathrm{F}}(f_j - f_{j+2})\right] - \frac{\gamma_{\mathrm{B}}}{2\beta_{\mathrm{B}}} D_{j-1}^{\mathrm{B}}, \tag{34}$$

where the relations between the coefficients of the forward and backward stencils have been substituted to highlight the equivalent terms in the two stencils. The operation count associated with solving the above systems is essentially the same as the most efficient Thomas algorithm as described in [10]. For the fourth-order three-point scheme a total of four multiplications and six additions are required per point, one addition per point more than the most optimized Thomas algorithm. For the fourth-order five-point scheme a total of five multiplications and nine additions are required per point, two more additions than the most efficient Thomas algorithm. For later comparisons we note that the explicit fourth-order DRP scheme requires a total of three multiplications and five additions to evaluate the first spatial derivative at a given point.

3.1. Numerical stability

To ascertain the global order of accuracy and demonstrate the stability characteristics of the boundary closures combined with the interior optimized prefactored compact schemes we consider the one-dimensional scalar wave equation,

$$\frac{\partial u}{\partial t}+\frac{\partial u}{\partial x}=0, \quad -1\leqslant x\leqslant 1, \quad t\geqslant 0, \tag{35}$$

subject to the following initial and boundary conditions:

$$u(x,0)=\sin(2\pi x), \quad u(-1,t)=\sin(2\pi(x-t)). \tag{36}$$

Eq. (35) is solved over the domain $-1\leqslant x\leqslant 1$ using a range of progressively finer uniform meshes. The interior schemes are combined with the boundary stencils of Section 2.4 and the solutions are integrated to long times, whilst the solution is examined for boundedness (asymptotic stability). Also the computational grid is refined while keeping the CFL number fixed, and convergence of the solution established (Lax stability). Consistent with the method of lines approach, the compact schemes are first used to discretize the spatial operators, before a fourth-order, four-stage Runge–Kutta scheme is used to integrate the equations forward in time. The L_2 error, $\sqrt{1/N\sum_{j=1}^{N}(u_j-u_{\text{exact}})^2}$, is then examined for boundedness. Where u_{exact} is the exact solution to this initial boundary value problem and is given by,

$$u_{\text{exact}}(x,t)=\sin(2\pi(x-t)). \tag{37}$$

The simulations were run to a time $T=100$ with a CFL number of unity. In each case the errors remained bounded and the simulations were characterized by nearly constant levels of error on all grids. Reducing the CFL number was found to only weakly influence the results, confirming that the observed errors are essentially only due to the spatial discretization schemes. The L_2 errors at time $T=100$ for both the fourth-order schemes are shown in Fig. 3 for various grid densities. In both cases it may be seen that the error decays

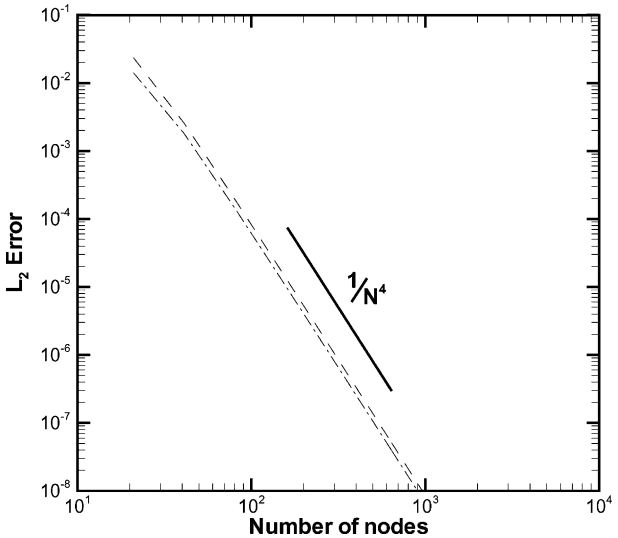

Fig. 3. L_2 solution errors: convergence rate of fourth-order schemes. (—) Idealized convergence rate, (- - -) fourth-order compact scheme (three-point stencil), (– · – · –) fourth-order compact scheme (five-point stencil).

in accordance with the idealized (fourth-order) convergence rate, and the fourth-order five-point scheme exhibits errors of a lower absolute value. The third-order boundary closures presented are therefore sufficient to ensure fourth-order global accuracy. We note that efforts to derive higher-order boundary closures, by matching the Taylor series of the interior schemes to higher-order, failed to yield stable systems.

3.2. Eigenvalue analysis

To confirm the findings of the previous section an eigenvalue analysis is performed to verify the boundary closures do indeed yield asymptotically stable solutions. We begin by considering

$$\frac{\partial u}{\partial t} + c\frac{\partial u}{\partial x} = 0 \tag{38}$$

over the domain $x \in [0,1]$ with the prescribed inflow boundary condition $u(0,t) = g(t)$. The domain is divided into N uniform intervals of width Δx, where $N\Delta x = 1$. The application of either of the compact spatial operators to Eq. (38) yields a system of ODEs which may be written:

$$\frac{\mathrm{d}\mathbf{U}}{\mathrm{d}t} = -\frac{c}{\Delta x}\mathbf{M}\mathbf{U} + \mathbf{B}g(t). \tag{39}$$

Here $\mathbf{M}$ is a $N \times N$ matrix, defined such that $\mathbf{U}_x = \mathbf{M}\mathbf{U}$, and $\mathbf{U}$ is an N-dimensional vector representing the values of the function at the nodal points. $\mathbf{B}$ is a vector of dimension N. For the purpose of stability analysis we note that $g(t)$ may be set to zero with little loss of generality [13]. The eigenvalues of $\mathbf{M}$ determine the asymptotic stability of the system of ODEs. These are in general complex valued and depend on the size of the matrix $\mathbf{M}$, the interior differencing scheme and the boundary scheme. For numerical stability it is required that all eigenvalues of $\mathbf{M}$ lie in the left half of the complex plane. The matrix $\mathbf{M}$ is determined as follows for the prefactored compact schemes. Firstly, the boundary expressions and interior schemes are combined to eliminate $(u_0)_x^{\mathrm{F}}$ and $(u_0)_x^{\mathrm{B}}$ from the system of equations. Through the application of the boundary condition $g(t) = 0 = u_0$, the system of equations for the forward and backward derivatives $\mathbf{U}_x^{\mathrm{F}}$ and $\mathbf{U}_x^{\mathrm{B}}$ may be written as:

$$\mathbf{A}^{\mathrm{F}}\mathbf{U}_x^{\mathrm{F}} = \frac{1}{\Delta x}\mathbf{C}^{\mathrm{F}}\mathbf{U}, \tag{40}$$

$$\mathbf{A}^{\mathrm{B}}\mathbf{U}_x^{\mathrm{B}} = \frac{1}{\Delta x}\mathbf{C}^{\mathrm{B}}\mathbf{U}, \tag{41}$$

where the above system of equations is applied at nodes $j = 1$ to N. Using Eq. (11), $\mathbf{U}_x$ may then be expressed as

$$\mathbf{U}_x = \frac{1}{2}(\mathbf{U}_x^{\mathrm{F}} + \mathbf{U}_x^{\mathrm{B}}) = \frac{1}{2\Delta x}((\mathbf{A}^{\mathrm{F}})^{-1}\mathbf{C}^{\mathrm{F}} + (\mathbf{A}^{\mathrm{B}})^{-1}\mathbf{C}^{\mathrm{B}})\mathbf{U} \tag{42}$$

from which we find

$$\mathbf{M} = \frac{1}{2}((\mathbf{A}^{\mathrm{F}})^{-1}\mathbf{C}^{\mathrm{F}} + (\mathbf{A}^{\mathrm{B}})^{-1}\mathbf{C}^{\mathrm{B}}). \tag{43}$$

For the combinations of interior schemes and boundary stencils presented in this work the eigenvalues of $\mathbf{M}$ must be determined numerically. For this purpose we have used an eigenvalue solver from the LAPACK library. In all cases the matrix $\mathbf{M}$ was evaluated numerically, following the specification of the matrices $\mathbf{A}^{\mathrm{F}}$, $\mathbf{C}^{\mathrm{F}}$, $\mathbf{A}^{\mathrm{B}}$ and $\mathbf{C}^{\mathrm{B}}$ appropriate to the interior scheme and boundary closure being considered. This was carried

out for three different values of N, namely 26, 51 and 101. Figs. 4 and 5 illustrate the eigenvalues obtained for the two schemes with their respective boundary closures. As may be seen in both cases the combinations of interior stencil and boundary closures yield eigenvalues with negative real parts, and therefore satisfy the stability constraint.

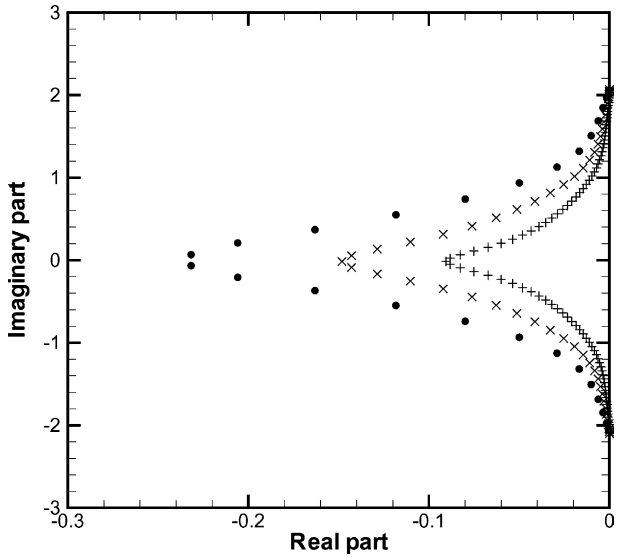

Fig. 4. Eigenvalue spectrum fourth-order three-point stencil scheme with third-order boundary closure: (●) $N = 26$; (×) $N = 51$; (+) $N = 101$.

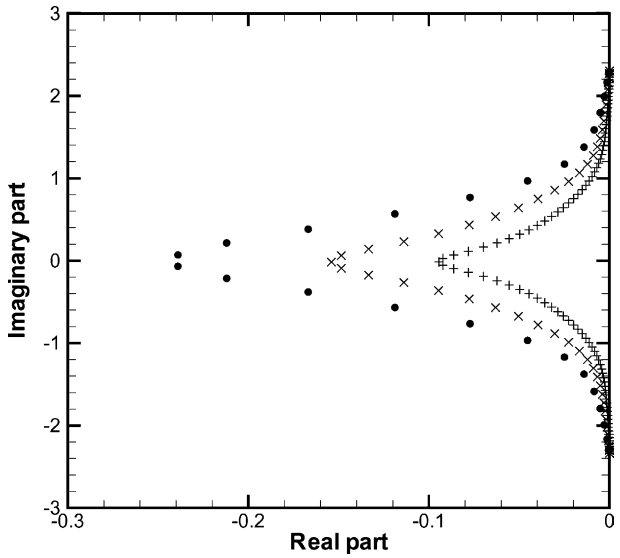

Fig. 5. Eigenvalue spectrum fourth-order five-point stencil scheme with third-order boundary closure: (●) $N = 26$; (×) $N = 51$; (+) $N = 101$.

4. Applications

In this section we illustrate the properties of the derived schemes through their application to several benchmark problems. These problems are taken from the First [14] and Second [15] Workshops on Benchmark problems for Computational Acoustics.

4.1. Linear wave propagation

In this first problem we consider the one-dimensional convection of an initial Gaussian disturbance. This problem is governed by the simple wave equation:

$$\frac{\partial u}{\partial t}+\frac{\partial u}{\partial x}=0, \tag{44}$$

where

$$\begin{aligned} &u(x,0)=\frac{1}{2}\mathrm{e}^{-\ln(2)(x-30)^2/2},\\ &\Delta x=1, \quad 0\leqslant x\leqslant 300. \end{aligned} \tag{45}$$

It should be noted that the initial Gaussian distribution specified here differs from that specified in the original problem. The distribution given here has a smaller half width, providing a more challenging case by raising the wavenumber content of the initial disturbance.

The numerical simulations are performed using the optimized compact schemes to evaluate the spatial derivative. Temporal integration is performed using the 4–6 low dispersion and dissipation Runge–Kutta (LDDRK) optimized scheme of Hu et al. [16]. This is a two-step alternating scheme in which different coefficients are employed in the alternating steps. The 4–6 notation signifies four stages are used for the first time step and six stages for the second time step in the cycle. The low-storage implementation of this scheme is employed in this work. This results in a scheme which is fourth-order accurate in time for linear problems and second-order accurate for non-linear problems. When combined with the fourth-order three-point compact stencil, the scheme is stable to a CFL limit of 1.199. When combined with the fourth-order five-point compact stencil, the scheme is stable to a CFL limit of 1.011. To ensure the errors observed in the simulations are essentially due only to the spatial discretization scheme employed we employ in this problem a time-step size well below that imposed by stability considerations ($\Delta t = 0.01$). The solutions obtained after 20,000 time-steps are shown in Fig. 6 for Tam's DRP scheme, Hixon's prefactored sixth-order scheme, the optimized fourth-order three-point prefactored compact scheme, and the fourth-order five-point prefactored compact scheme. It may be seen that under these severe initial conditions the DRP scheme suffers from considerable dispersion error. The sixth-order compact scheme shows less error, but is seen to perform less well than the fourth-order, three-point optimized scheme. However, as one would anticipate from the previous analysis, the best performance is observed with the fourth-order, five-point optimized compact scheme.

From these results it is evident that the optimized prefactored compact schemes have reduced grid resolution requirements in comparison to both the explicit and un-optimized prefactored compact schemes. To gauge the overall efficiency of these schemes it is important to consider the associated memory and computational costs. The relative importance of these two factors is problem dependent. In the context of the current problem, numerical experiments indicate the explicit fourth-order scheme requires 1.85 more grid points to achieve a level of accuracy comparable to that of the fourth-order five-point prefactored compact scheme. Similarly, the sixth-order and fourth-order three-point prefactored schemes require 1.45 and 1.25 more grid points, respectively. The relative cost of the various schemes may be assessed by

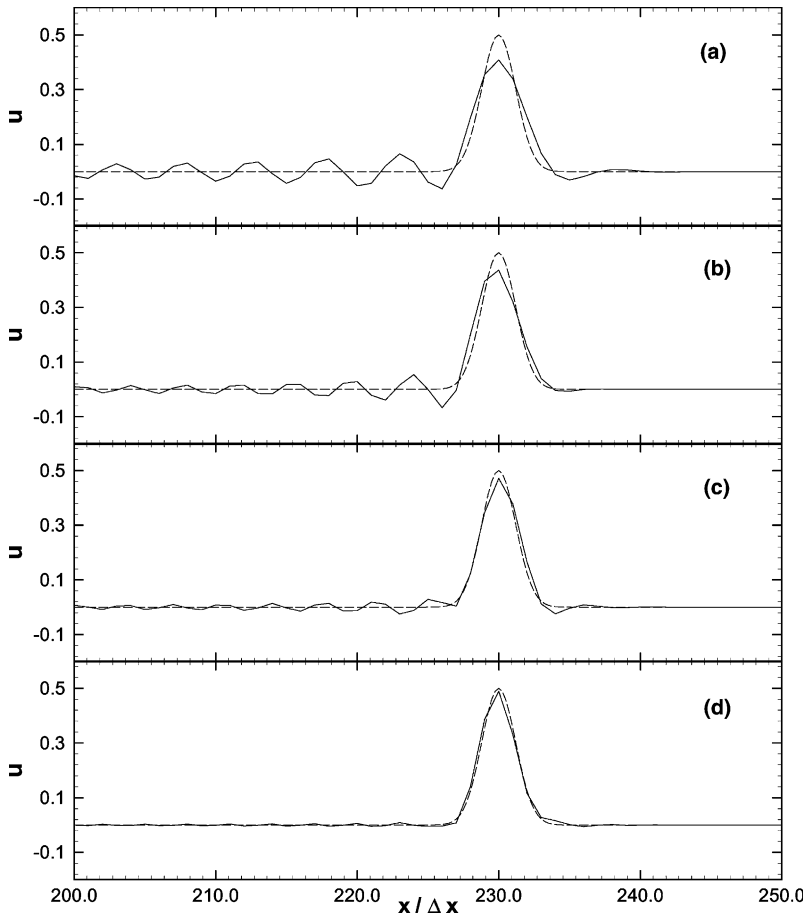

Fig. 6. Comparison between computed and exact solutions of the simple one-dimensional wave equation. (a) Fourth-order DRP scheme (seventh-point stencil). (b) Sixth-order compact scheme (three-point stencil). (c) Fourth-order compact scheme (three-point stencil). (d) Fourth-order compact scheme (five-point stencil). (—) Numerical solution, (- - -) exact solution.

considering the operation count per node. The explicit fourth-order DRP scheme requires a total of eight operations, whereas the implicit prefactored three- and five-point schemes require 10 and 14 operations, respectively. The three- and five-point implicit schemes are therefore approximately 1.25 and 1.75 times more expensive than the explicit fourth-order scheme. On the basis of this simplified analysis it may be concluded that the gain in resolution obtained through the use of the optimized prefactored schemes outweighs the associated greater computational overheads, and the fourth-order three-point scheme offers the best performance in terms of resolution versus computational cost.

4.2. Two-dimensional acoustic scattering

To demonstrate the accuracy of the derived schemes in multi-dimensions and illustrate the use of the derived boundary stencils we consider as a second example a two-dimensional acoustic scattering problem from the Second CAA workshop. The physical problem is to find the propeller generated sound field scattered off the fuselage of an aircraft. The fuselage is idealized as a circular cylinder and the noise source

(propeller) as a line source so that the computation problem is two-dimensional. The two-dimensional cylinder has a radius of $R = 0.5$ and is located at the origin. At time $t = 0$, the initial conditions are $u = v = 0$, and

$$p(x, y, 0) = \exp\left[- \ln 2 \left(\frac{(x-4)^2 + (y)^2}{0.04} \right) \right]. \tag{46}$$

The problem asks for the unsteady pressure time history at three points $A(r = 5, \theta = 90°)$, $B(r = 5, \theta = 135°)$ and $C(r = 5, \theta = 180°)$, over the time interval $t = 6 \rightarrow 10$. We find the solution to this problem by solving the linearized Euler equations in polar coordinates:

$$\frac{\partial}{\partial t} \begin{bmatrix} u_r \\ u_\theta \\ p \end{bmatrix} + \frac{\partial}{\partial r} \begin{bmatrix} p \\ 0 \\ u_r \end{bmatrix} + \frac{1}{r} \frac{\partial}{\partial \theta} \begin{bmatrix} 0 \\ p \\ u_\theta \end{bmatrix} = \frac{1}{r} \begin{bmatrix} 0 \\ 0 \\ u_r \end{bmatrix}. \tag{47}$$

All the numerical computations were performed over a domain extending radially from $R = 0.5$ to $R = 10.5$, and over the entire azimuthal plane with θ ranging from 0 to 2π. A total of 81 and 149 mesh points were employed in the radial and azimuthal directions, respectively. A CFL number of 0.5 was employed in all simulations. Three boundary conditions were used: a wall condition on the cylinder at $r = 0.5$, an acoustic radiation condition along the external domain boundary at $r = 10.5$, and a periodic condition along both azimuthal boundaries at $\theta = 0$ and $\theta = 2\pi$. The solid wall boundary condition follows the implementation of Hixon [10]. The radiation condition applied along the far field boundary is the acoustic radiation condition of Bayliss and Turkel [17]. The radial derivatives at the outer boundary are computed using one-sided boundary stencils. Along the periodic boundaries the explicit 11-point stencils are used to start and end the sweeps in the azimuthal direction. The stencil uses data from both sides of the periodic boundaries. As the problem is solved in serial on a single processor no overlap is required between the adjacent boundaries to use the 11-point explicit stencil.

The mesh used in the simulations is shown partially in Fig. 7, alongside a snapshot of the computed pressure field at time $t = 6.37$. At this time the acoustic pulse has already impinged upon the cylinder

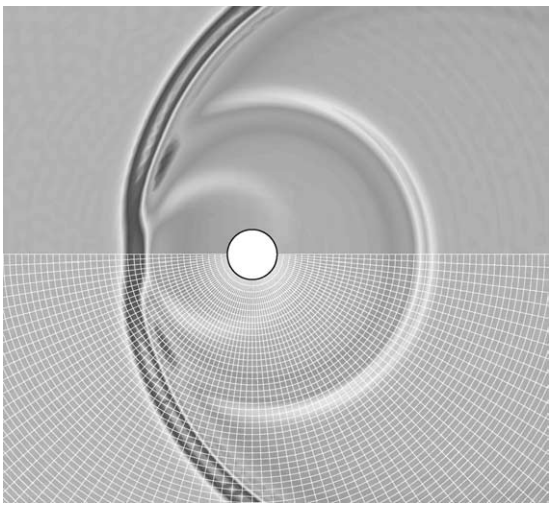

Fig. 7. Instantaneous pressure contours at time $t = 6.37$.

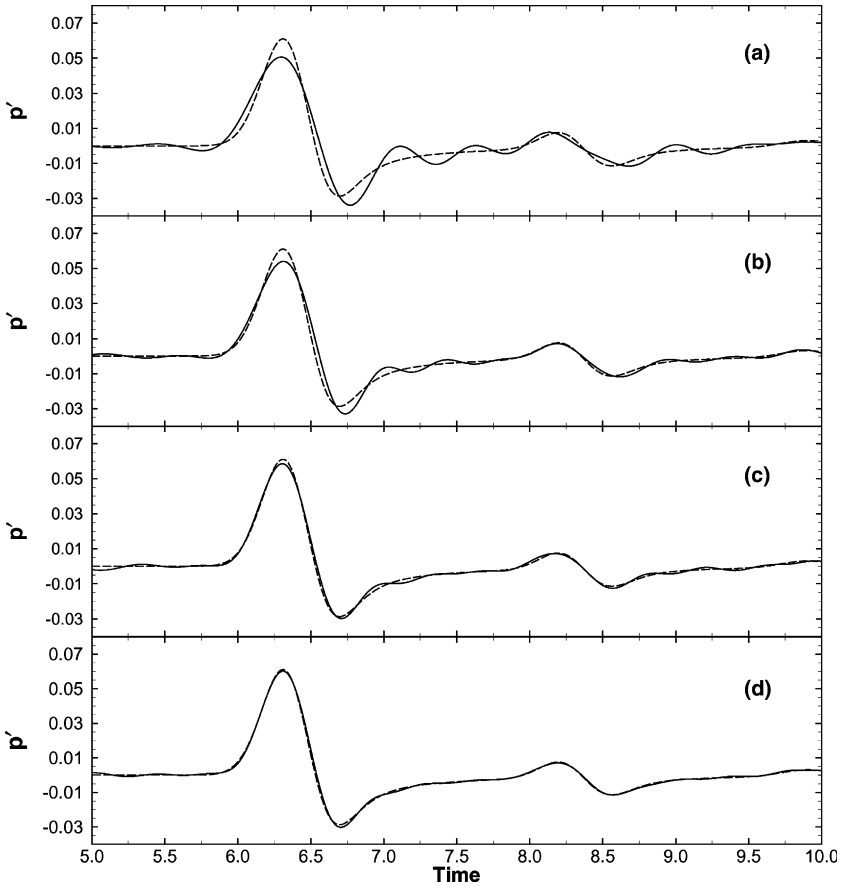

Fig. 8. Comparison between computed and exact solutions of two-dimensional scattering problem at A ($r = 5$, $\theta = 90°$). (a) Fourth-order DRP scheme (seven-point stencil). (b) Sixth-order compact scheme (three-point stencil). (c) Fourth-order compact scheme (three-point stencil). (d) Fourth-order compact scheme (five-point stencil). (—) Numerical solution, (- - -) exact solution.

generating the reflections evident in the solution field. Fig. 8 compares the solutions obtained using the same schemes as employed in the previous test case with the exact solution at the point $A(r = 5, \theta = 90°)$. As with the previous test case the superior resolution characteristics of the optimized prefactored schemes are evident. To verify similar accuracy is obtained irrespective of direction, Fig. 9 shows the pressure time histories computed using the optimized fourth-order, five-point scheme at the three observer locations, alongside the exact solutions. As may be seen, good agreement is evident at all three locations.

5. Conclusions

A strategy for developing prefactored compact schemes has been presented. The approach facilitates the optimization of the biased stencils for the simulation of wave phenomena. The procedure employs Fourier analysis and the concept of a numerical wavenumber to determine the coefficients of the biased stencils. The optimized prefactored compact schemes have smaller stencil sizes and require only the solution of two independent bi-diagonal matrices. Third-order accurate boundary stencils have been presented for the

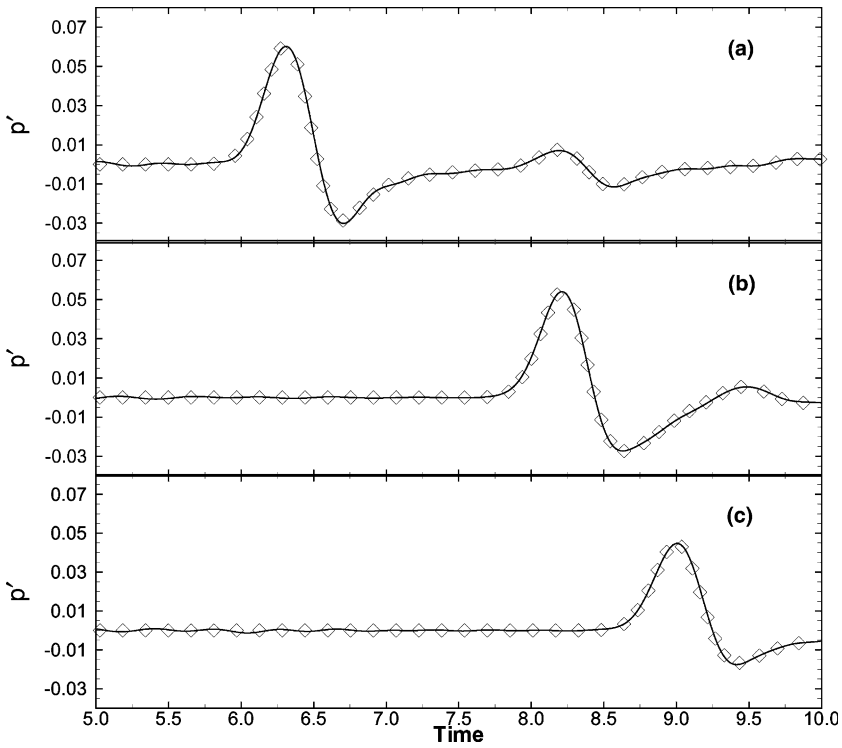

Fig. 9. Comparison between computed and exact solutions of two-dimensional scattering problem. (a) Pressure time history at A ($r = 5$, $\theta = 90°$). (b) Pressure time history at B ($r = 5$, $\theta = 135°$). (c) Pressure time history at C ($r = 5$, $\theta = 180°$). (—) Fourth-order compact scheme (five-point stencil), ($\diamondsuit$) analytic solution.

optimized prefactored compact schemes. The stability of these explicit boundary closures combined with the implicit interior schemes has been shown through numerical applications and eigenvalue analysis. The favourable characteristics of the developed schemes have been demonstrated through their application to single- and multi-dimensional benchmark problems.

References

[1] C.K.W. Tam, Computational aeroacoustics: issues and methods, AIAA J. 33 (1995) 1788.
[2] D. Gaitonde, J.S. Shang, Optimized compact-difference-based finite-volume schemes for linear wave phenomena, J. Comput. Phys. 138 (1997) 617.
[3] D.V. Nance, K. Viswanathan, L.N. Sankar, Low-dispersion finite volume scheme for aeroacoustic applications, AIAA J. 35 (1997) 255.
[4] C.K.W. Tam, J.C. Webb, Dispersion relation preserving finite difference schemes for computational acoustics, J. Comput. Phys. 107 (1993) 262.
[5] M. Zhuang, R.F. Chen, Optimized upwind dispersion-relation-preserving finite difference schemes for computational aeroacoustics, AIAA J. 36 (1998) 2146.
[6] R. Hixon, A New Class of Compact Schemes, AIAA Paper 98-0367, 1998.
[7] K.W. Thompson, Time-dependent boundary conditions for hyperbolic systems, J. Comput. Phys. 68 (1987) 1.
[8] C.K.W. Tam, Z. Dong, Wall boundary conditions for high-order finite difference schemes in computational aeroacoustics, Theor. Comput. Fluid Dyn. 6 (1994) 303.
[9] S.K. Lele, Compact finite difference schemes with spectral-like resolution, J. Comput. Phys. 103 (1992) 16.
[10] R. Hixon, Prefactored small-stencil compact schemes, J. Comput. Phys. 165 (2000) 522.

[11] R. Hixon, E. Turkel, High-accuracy compact MacCormack-type schemes for computational aeroacoustics, NASA CR 1998-208672, 1998.
[12] J.W. Kim, D.J. Lee, Optimized compact finite difference schemes with maximum resolution, AIAA J. 34 (1996) 887.
[13] M.H. Carpenter, D. Gottlieb, S. Abarbanel, The stability of numerical boundary treatments for compact high-order finite-difference schemes, J. Comput. Phys. 108 (1993) 272.
[14] J.C. Hardin, J.R. Ristorcelli, C.K.W. Tam (Eds.), ICASE/LaRC Workshop on Benchmark Problems in Computational Aeroacoustics, NASA CP-3300, 1995.
[15] C.K.W. Tam, J.C. Hardin (Eds.), Second Computational Aeroacoustics Workshop on Benchmark Problems, NASA CP-3352, 1997.
[16] F.Q. Hu, M.Y. Hussaini, J. Manthey, Low-dissipation and -dispersion Runge–Kutta schemes for computational acoustics, J. Comput. Phys. 124 (1996) 177.
[17] A. Bayliss, E. Turkel, Far field boundary conditions for compressible flows, J. Comput. Phys. 48 (1982) 182.